



## Article

# A Universal Multi-Frequency Micro-Resistivity Array Imaging Method for Subsurface Sensing

Haining Yang<sup>1</sup> , Yuting Liu<sup>1</sup>, Tingjun Li<sup>1,\*</sup>, Shijia Yi<sup>1</sup> and Na Li<sup>2</sup>

<sup>1</sup> School of Electronic Science and Engineering, University of Electronic Science and Technology of China (UESTC), Chengdu 611731, China; hnyang@uestc.edu.cn (H.Y.); 202122021130@std.uestc.edu.cn (Y.L.); yishijia@std.uestc.edu.cn (S.Y.)

<sup>2</sup> School of Information and Communication Engineering, University of Electronic Science and Technology of China (UESTC), Chengdu 611731, China; nali@uestc.edu.cn

\* Correspondence: tjli@uestc.edu.cn

**Abstract:** In this paper, a universal multi-frequency micro-resistivity array imaging (UMMAI) system for subsurface sensing is developed and verified. Different from conventional micro-resistivity imaging equipments, UMMAI is capable to provide high-resolution fullbore formation images in multiple logging environments including an oil-based mud scene, water-based mud scene and water-oil mixed mud scene, owing to the large dynamic range and good linearity of transceivers. With the advantage of diversity in excitation signal frequency, UMMAI presents abundant amplitude-frequency characteristics response images and phase-frequency characteristics response images of subsurface formations at the same time, which is beneficial to multi-frequency image fusion in the future. The fullbore imaging ability of UMMAI is evaluated in three different field tests, and the results show that UMMAI can give satisfactory credible formation images with high resolution, which is suitable for subsurface formation discrimination and useful for reservoir identification.

**Keywords:** micro-resistivity; array imaging; high resolution; well logging



**Citation:** Yang, H.; Liu, Y.; Li, T.; Yi, S.; Li, N. Universal Multi-Frequency Micro-Resistivity Array Imaging Method for Subsurface Sensing. *Remote Sens.* **2022**, *14*, 3116. <https://doi.org/10.3390/rs14133116>

Academic Editors: Tien Yin Chou and Gianluca Gropelli

Received: 8 June 2022  
Accepted: 26 June 2022  
Published: 28 June 2022

**Publisher's Note:** MDPI stays neutral with regard to jurisdictional claims in published maps and institutional affiliations.



**Copyright:** © 2022 by the authors. Licensee MDPI, Basel, Switzerland. This article is an open access article distributed under the terms and conditions of the Creative Commons Attribution (CC BY) license (<https://creativecommons.org/licenses/by/4.0/>).

## 1. Introduction

As one of the most important applied geophysical methods, well logging provides geophysical parameters by using the electrochemical properties, electrical conductivity and acoustic properties of rock formations [1–5].

Currently, there are mainly three well logging approaches: acoustic logging [6,7], nuclear logging [8,9] and electrical logging [10,11]. Acoustic logging makes use of the characteristics of acoustic wave propagation in different formations to obtain the geological characteristics such as subsurface holes, cracks, collapses and debris [12–14]. The acoustic logging result is susceptible to the acoustic frequency, filling mud parameters and well diameter. High acoustic frequency, large mud density and well diameter will lead to the decline of logging quality.

Nuclear logging takes advantages of the nuclear magnetic resonance characteristics of hydrogen nucleus in the formation fluid, which is capable to provide formation parameters accurately and timely [15,16]. However, it suffers from the randomness and uncertainty in fluid identification, and is vulnerable to large mud resistivity, high temperature and low signal-to-noise ratio. Besides, its logging speed and logging cost need to be improved.

Electrical logging obtains the formation resistance information by measuring the current flowing through the formation from receiving electrodes [17–19]. The changes in surrounding well formation can cause changes in the electrode current, which can reflect the heterogeneity of lithology or electrochemical in the formation at the receiving electrodes [20–23]. The sample collect board can be placed closed to the borehole wall to reduce the signal power loss.

With the development of array imaging, micro-resistivity array imaging system [24–26] can obtain a variety of rich formation information in circumferential direction and radial

direction of the borehole, which is suitable for the exploration and development of complex concealed oil and gas reservoirs [27–29]. One of the most widely used micro-resistivity imaging tool is the formation micro scanner, which was developed by Schlumberger in the 1980s. In 1990s, the fullbore formation micro imager was released, which is significantly improved in borehole coverage and resolution, and is widely used in geological interpretation and oil and gas evaluation. Considering the subsurface formation resistivity that varies widely and various filling mud in different logging scenarios, current micro-resistivity array imaging system needs to improve versatility and frequency flexibility.

In this paper, a universal multi-frequency micro-resistivity array imaging (UMMAI) system for subsurface sensing is introduced and its imaging performance is evaluated. By optimizing the receive chain design, UMMAI provides real-time data acquisition and high resolution imaging of subsurface formation. The system can work in three modes: operative mode, calibration mode, and self-checking mode. A stratigraphic simulation system is also built for UMMAI test convenience, which can simulate the variation of the stratigraphic impedance. A direct digital frequency synthesis (DDS) device is used as the waveform generator to produce multiple high-resolution low-distortion sine signals ranging from 1 kHz to 20 MHz under the control of field programmable gate array (FPGA). With the aid of large dynamic range of receiver array and good linearity of transmitter, UMMAI is verified capable to handle the formation imaging in multiple logging environments including oil-based mud scene, water-based mud scene and water-oil mixed mud scene, which is promising to deal with the reservoir identification such as fractures, dissolved pores and holes.

This rest of the paper is organized as follows. The methodology and modeling of UMMAI are described in Section 2. In Section 3, a detailed description of UMMAI and performance tests are given. Finally, the comprehensive summarization of UMMAI performance and its array imaging capabilities are concluded in Section 4.

## 2. Methodology

Firstly, the circuit model of the imaging array is established, as shown in Figure 1. There are one transmitter electrode and a receiver array in the UMMAI system. The receiver array is composed of  $N$  receiver electrodes, which are set around the borehole. The real stratum impedance in the  $n$ th receiving chain is represented as  $Z_{Xn}$ , while  $n = 1, 2, \dots, N$ . The excitation internal resistance is denoted as  $R_S$ . In the actual measurement of the stratum impedance, the borehole is commonly filled with mud fluid and the gaps between electrodes and stratum cannot be negligible. The gap mud impedances between receiver electrodes and stratum are denoted as  $Z_{Rn}$ . The gap mud impedances between transmitter electrode and stratum is denoted as  $Z_T$ . Besides, the parasitic capacitance in the circuit is represented as  $C_W$ , which is usually ignored in low frequency applications.

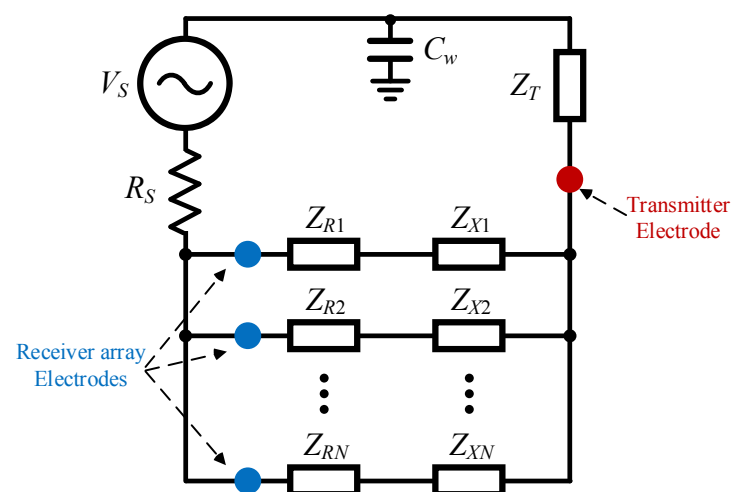
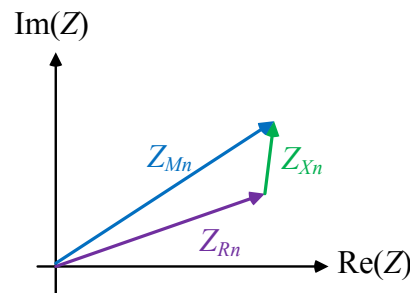


Figure 1. The circuit model of UMMAI imaging system.

Considering the existence of  $R_S$ ,  $Z_T$  and  $Z_{Rn}$ , the measured stratum impedance in the  $n$ th receiving chain,  $Z_{Mn}$ , can be represented as follows,

$$Z_{Mn} = R_S + Z_T + Z_{Rn} + Z_{Xn}. \quad (1)$$

In Equation (1), the impedance  $Z_T$  is a capacitive impedance and its influence can be suppressed by increasing the area of transmitter electrode and signal frequency. The internal resistance  $R_S$  can be reduced to a small enough value by optimizing source design. Therefore, the relations between impedances  $Z_{Mn}$ ,  $Z_{Rn}$  and  $Z_{Xn}$  can be described in Figure 2.



**Figure 2.** The relations between impedances  $Z_{Mn}$ ,  $Z_{Rn}$  and  $Z_{Xn}$ .

Assuming that the dielectric constant  $\epsilon$  of mud fluid remains unchanged, the area of the transmitter electrode is  $S$ , the distance between the emission electrode and the formation is  $d$ , and the resistivity of mud fluid is  $\rho$ , the equivalent resistance of mud fluid can be expressed as:

$$r = \frac{\rho \cdot d}{S} \quad (2)$$

The equivalent capacitance of mud fluid can be expressed as:

$$C = \frac{\epsilon \cdot S}{d} \quad (3)$$

Then  $Z_{Rn}$  is the complex impedance in parallel with  $r$  and  $C$ :

$$Z_{Rn}(\omega) = r \parallel \frac{1}{j\omega C} = \frac{r}{1 + j\omega r C} \quad (4)$$

The modulus and phase of  $Z_{Rn}$ ,  $|Z_{Rn}|$  and  $\theta_n$  can be represented as:

$$|Z_{Rn}(\omega)| = \frac{r\sqrt{1 + \omega^2 r^2 C^2}}{1 + \omega^2 r^2 C^2} = \frac{\rho d \sqrt{1 + \omega^2 \rho^2 \epsilon^2}}{S(1 + \omega^2 \rho^2 \epsilon^2)} \quad (5)$$

$$\theta_n(\omega) = -\arctan(\omega r C) = -\arctan(\omega \rho \epsilon) \quad (6)$$

$|Z_{Rn}|$  and  $\theta_n$  can be obtained in a priori measurement according to the gap and mud parameters. So the value of  $Z_{Xn}$  can be inferred with the measured  $Z_{Mn}$  and  $Z_{Rn}$ .

In the normal working mode, the excitation source  $V_S$  produces multiple excitation signals with different frequencies, which enter the stratum through transmitter electrode and received by  $N$  receiver electrodes. The changes in stratum impedance  $Z_{Xn}$  induces the change in chain current. The measured impedance of  $n$ th receiving chain  $Z_{Mn}$  can be obtained by sampling the  $n$ th chain current. Since it is difficult to measure the amplitude and phase of chain current directly, the chain current is generally converted to a voltage signal using a stable sampling resistor. Therefore, the real stratum impedance  $Z_{Xn}$  can be inferred with the measured voltage amplitude and phase of sampling resistor.

### 3. Result and Discussion

#### 3.1. System Design

Firstly, the system design description of UMMAI system for well logging is given. UMMAI mainly consists of a transmitter unit, 6 signal acquisition pads and a control-processing unit. A stratigraphic simulation system is also built for UMMAI test convenience, which can simulate the variation of the stratigraphic impedance. The schematic architecture of UMMAI is shown in Figure 3. As shown in Figure 3, the control-processing unit and transmitter unit are located in the heat resistant cylinder case of the instrument, the acquisition units are located in the retractable pad plates. The pictures of control-processing unit, transmitter unit and signal acquisition unit in UMMAI are shown in Figure 4.

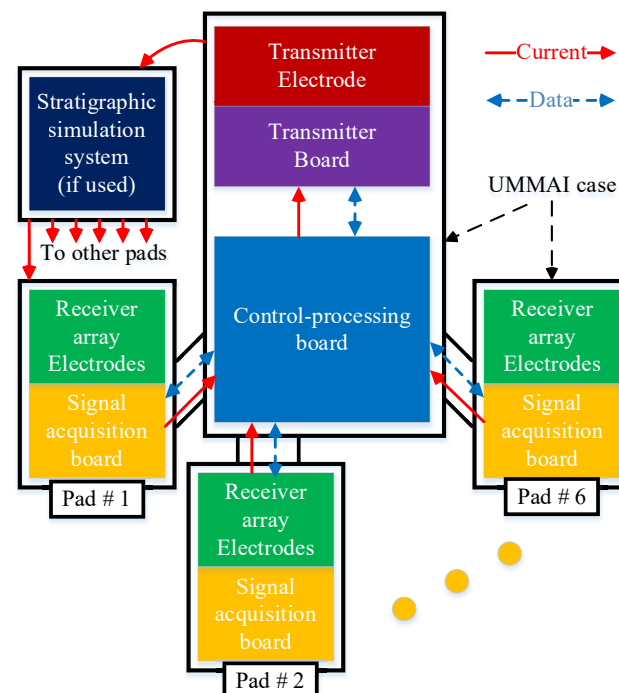


**Figure 3.** The simplified measurement equivalent circuit in actual measurement environment.

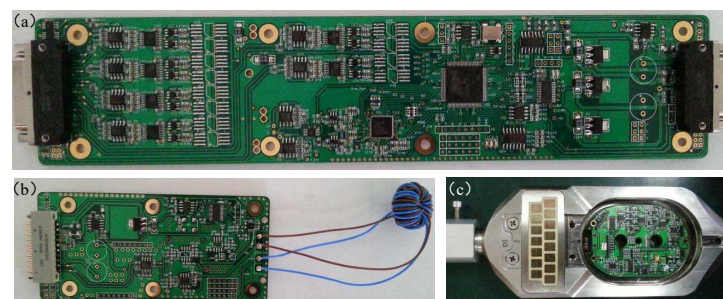


**Figure 4.** The pictures of (a) control-processing unit, (b) transmitter unit and (c) signal acquisition unit in UMMAI.

The system can work in three modes: operative mode, calibration mode, and self-checking mode. In operative mode, the UMMAI system is placed into a real well environment and the variable current amplitude and phase caused by the external mud and stratum is collected when the UMMAI moves along the well direction. In calibration mode, the stratigraphic simulation system is used instead of the real well environment, which can simulate the variable impedance environment via a known resistor array under the control of control-processing unit. In self-checking mode, the sine signals are directly looped into the control-processing unit, and the working state of the transmitter unit can be judged.

In the control-processing unit, a FPGA is selected as the master control device owing to its outstanding performance in wide operation temperature range, flexible programming characteristic and economical price. A DDS device is used as the waveform generator to produce high-resolution low-distortion sine signals ranging from 100 Hz to 20 MHz under the control of FPGA. Due to the insufficient driving power of control-processing unit, an transmitter unit with output power self detection function is designed to increase the driving ability. The produced signals are amplified in transmitter unit and sent to the transmitter electrode, either to drive the subsurface media or for self-checking purpose. The signal transmission line to transmitter electrode is wrapped on the magnetic ring to suppress the electromagnetic interference introduced by the multi-channel high-frequency signal transmission and working environment. In addition, the transmitting unit is also equipped with a self-check circuit to improve the efficiency of the circuit fault self-check.

The sine signals pass through the actual subsurface media or the stratigraphic simulation system, and received by the receiver array electrodes on 6 signal acquisition pads. The detection front-end of the data acquisition circuit first uses a negative feedback operational amplifier to convert the weak current signal to voltage signal for the subsequent signal amplification and filtering operations. The signals are processed in differential mode for the consideration of the common-mode signal rejection. Then the differential output signal of the data acquisition unit is sent to the control-processing unit, where the signal amplitude and phase are sampled by a logarithmic-amplifier-based ADC with a high dynamic range.

There are a front-end sampling circuit, a reconfigurable operational amplifier, a filter circuit and a difference transformation circuit on the control-processing unit. The signals from all data acquisition units are firstly amplified by the reconfigurable amplifier, the cut-off frequency and gain can be flexible configured by FPGA according to the frequency of transmitted signal and environment. In the previous tests, it was found that the amplified signals were greatly disturbed by the noise in the measurement environment, which affected the measurement results to some extent. After adding the post-stage filter circuit, the influence of noise is suppressed greatly and the signal-to-noise ratio is improved. The filtered signals are then sampled in time division multiplexing mode using a multi-channel multiple selection switch and converted into digital samples. The sampled data are framed and transmitted to the surface equipment via FPGA.

In order to achieve high precision and high reliability, the self-checking working mode is added in the UMMAI design. The multi-channel multiple selection switch can be selected to a known input channel, and the amplitude and phase of the channel current can be measured in real time, so the error caused by the non-ideal characteristics such as temperature drift can be evaluated and eliminated.

### 3.2. Lab Experiment

The formation impedance to be measured commonly varies widely from several hundred ohms to mega ohms. Therefore, the designed UMMAI system is required to have excellent sensitivity, good linearity, high reliability and large dynamic range to adapt to the changes of the subsurface environment.

Firstly, the linearity of UMMAI system output is verified. UMMAI works in the self-checking working mode and three sine excitation signals with frequencies of 100 kHz, 1 MHz and 10 MHz are used. The excitation signal is divided into two signals: the first signal is sent to the transmitter electrode, the second signal is used as the reference signal in sample amplitude and phase calculation. The amplitudes and phases of samples under different signal frequencies, chain gains, transmitter phase shifts and transmitter attenuations are collected and displayed in Figures 5 and 6, in which G stands for the gain of receiving chain and P represents the phase of transmitted signal.

As shown in Figure 5a,b, the normalized sample amplitudes remains almost unchanged when the phase of transmitted signal changes between  $0^\circ$  and  $90^\circ$ , no matter whatever excitation signal frequency and chain gain are used. When the excitation signal frequency increases to 10 MHz and the chain gain is set as 30 dB in Figure 5c, the differences of normalized sample amplitudes between different transmitted signal phase increases to

1.7 dB, which can be ignored in the following impedance analysis. The results show that the amplitudes of collected samples are immune to the phase of transmitted signal.

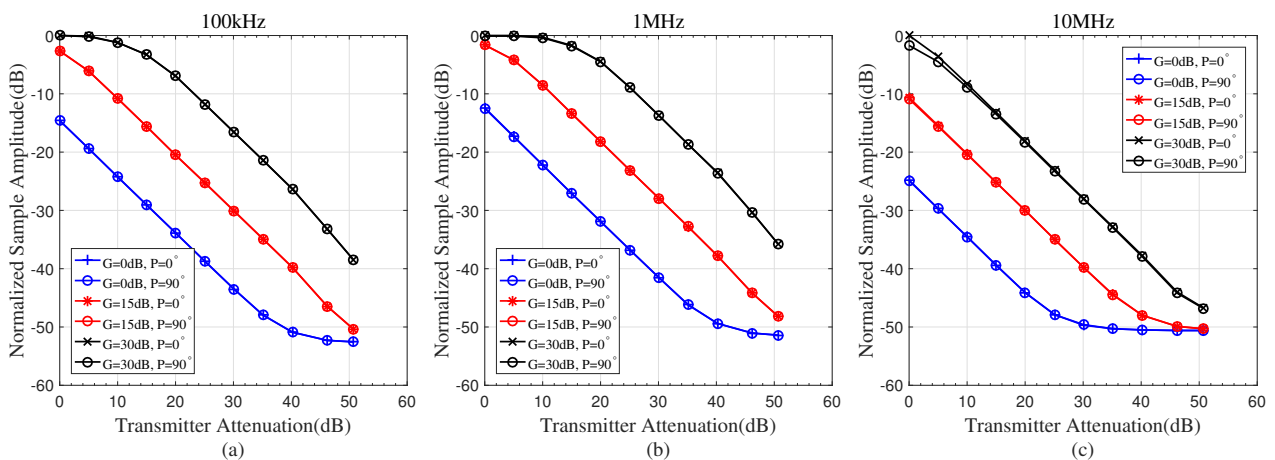


**Figure 5.** The normalized amplitudes of samples at different chain gains and transmitter phase shifts when the excitation signal frequency is (a) 100 kHz, (b) 1 MHz and (c) 10 MHz, respectively. G stands for the gain of receiving chain and P represents the phase of transmitted signal.

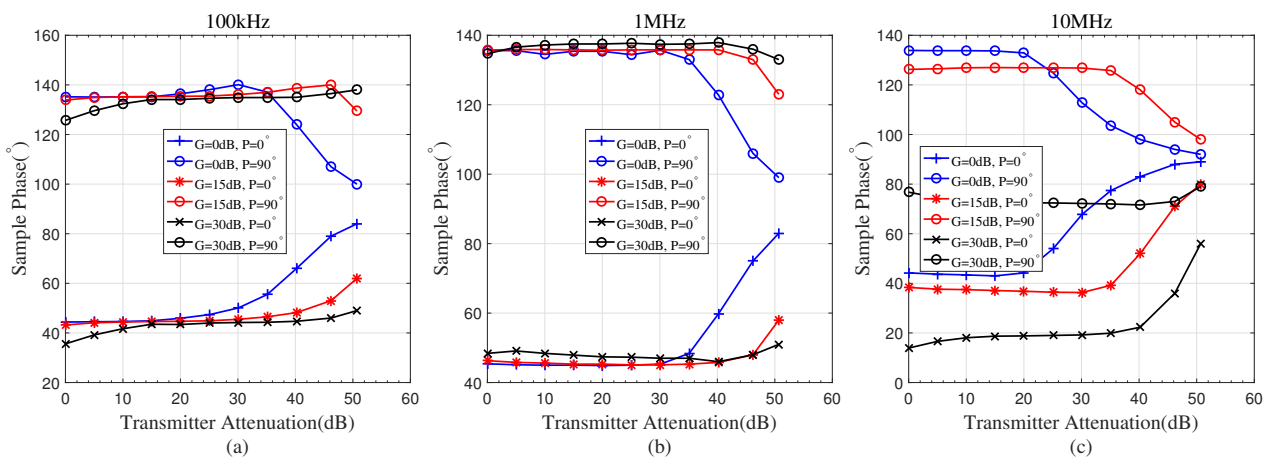


**Figure 6.** The phases of samples at different chain gains and transmitter phase shifts when the excitation signal frequency is (a) 100 kHz, (b) 1 MHz and (c) 10 MHz, respectively. G stands for the gain of receiving chain and P represents the phase of transmitted signal.

Moreover, the results in Figure 5a show the UMMAI receiver chain can achieve a linear dynamic range no less than 50 dB when the chain gain is set as 15 dB. When the transmitter attenuation is larger than 35 dB, the linear of receiver chain at  $G = 0$  dB is deteriorated due to the low signal-to-noise ratio. The linear of receiver chain at  $G = 30$  dB is also deteriorated when transmitter attenuation is less than 20 dB, which is caused by the nonlinear saturation of the receiver chain. Similar phenomenons happen when the excitation signal frequencies are 1 MHz and 10 MHz, as shown in Figure 5b,c, despite the nonlinearity degrees of receiver chain are different.

In Figure 6a, the sample phase changes with the transmitter attenuation obviously when the transmitter attenuation is larger than 30 dB, especially when the receiver chain gain is set as  $G = 0$  dB. This is mainly caused by the low signal-to-noise ratio at the receiver electrode. When the receiver chain gain increases to 15 dB and 30 dB, the differences between sample phase decrease to  $5^\circ$  and  $3^\circ$  while the transmitter attenuation is 50 dB and phase of transmitted signal is  $90^\circ$ . Similar phenomenons happen when the excitation signal frequency is 1 MHz, as shown in Figure 6b. The linearity of sample phase gives the worst performance when the excitation signal frequency increases to 10 MHz because of

the influence of high frequency parasitic components in transmitter and receiver chains on phase.

Next, the capability of linear resistance measurement of UMMAI system is verified. UMMAI works in the operative mode and four sine excitation signals with frequencies of 1 kHz, 10 kHz, 100 kHz and 1 MHz are used. Dozens of resistors with accurate resistances are used for evaluation. The amplitudes and phases of samples under different signal frequencies, chain gains and resistances are collected and displayed in Figure 7, in which G stands for the gain of receiving chain.

As shown in Figure 7a, the receiver chain can remain a linear dynamic range larger than 40 dB at  $G = 20$  dB when measuring the resistances from 1 k $\Omega$  to 200 k $\Omega$ . By selecting receiver gain reasonably and combining the samples at different gains, UMMAI can cover a linear resistance measurement range from 100  $\Omega$  to 2 M $\Omega$  using 1 kHz excitation signal. Figure 7b validates the similar linear resistance measurement ability of UMMAI when using 10kHz excitation signal. In Figure 7c, the linear resistance measurement range of UMMAI narrows to some extent due to poor high frequency response, which is from 100  $\Omega$  to 467.2 k $\Omega$ . The linear performance continues to deteriorate using 1 MHz excitation signal, while the linear resistance measurement range is from 100  $\Omega$  to 100 k $\Omega$ .

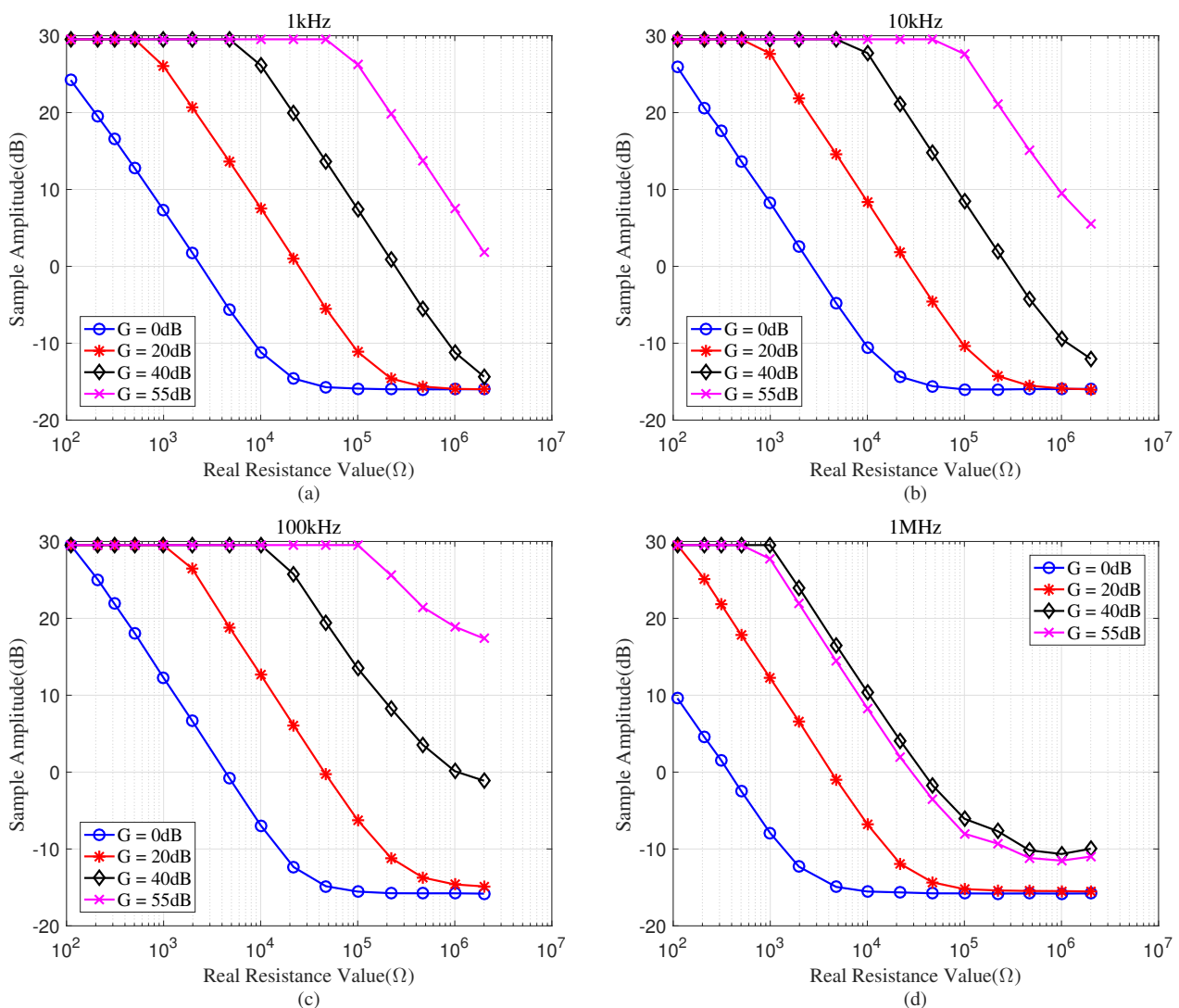


**Figure 7.** The amplitudes of samples in different resistor measurements when the excitation signal frequency is (a) 1 kHz, (b) 10 kHz, (c) 100 kHz and (d) 1 MHz, respectively. G stands for the gain of receiving chain.

Finally, the accurate performance of UMMAI resistance measurement is evaluated. UMMAI works in the operative mode and three sine excitation signals with frequencies of 100 kHz, 1 MHz and 10 MHz are used. Dozens of resistors with accurate resistances are used for evaluation. The measured resistance values of resistors and phases of samples under different signal frequencies, chain gains and resistances are collected and displayed in Figures 8 and 9, in which G stands for the gain of receiving chain.

As shown in Figure 8a, UMMAI can cover a linear resistance measurement range from 2 k $\Omega$  to 10 M $\Omega$  using 100 kHz excitation signal by selecting receiver gain reasonably and combining the samples at different gains, which is also the same using 1-MHz excitation signal in Figure 8b. The linearity of UMMAI reduces in Figure 8c, while the linear resistance measurement range is from 2 k $\Omega$  to 100 k $\Omega$  when using 10 MHz excitation signal. The results in Figure 9 show that the difference in sample phase is less than 5 $^\circ$  when the receiver chain of UMMAI achieves a good resistance measurement linearity, however, the sample phase consistency will deteriorate badly in non-linear resistance measurement range, especially when using high frequency excitation signal.

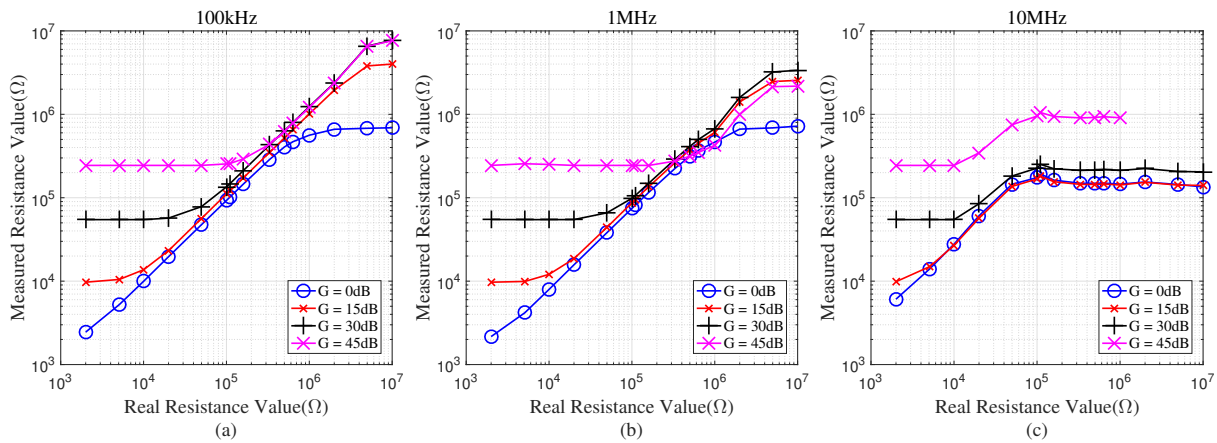


**Figure 8.** The measured resistance values in different resistor measurements when the excitation signal frequency is (a) 100 kHz, (b) 1 MHz and (c) 10 MHz, respectively. G stands for the gain of receiving chain.

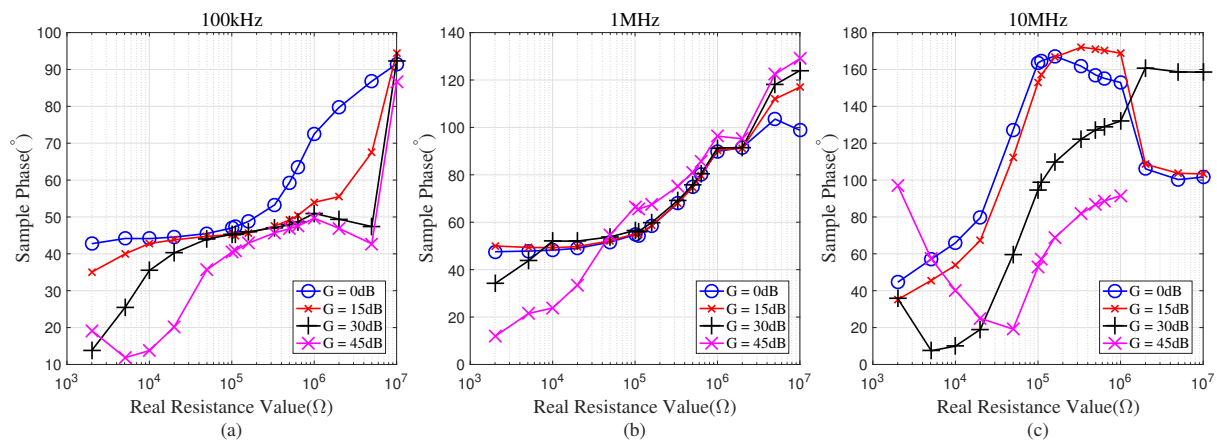


**Figure 9.** The sample phases in different resistor measurements when the excitation signal frequency is (a) 100 kHz, (b) 1 MHz and (c) 10 MHz, respectively. G stands for the gain of receiving chain.

### 3.3. Field Test

In this section, the array imaging performance of UMMAI is evaluated in three different field tests. In each field test, UMMAI is placed into a simulated borehole, the wall of which is engraved with various patterns, as is shown in Figure 10. UMMAI works in the operative mode and three sine excitation signals with frequencies of 200 kHz, 1 MHz and 5 MHz are used.



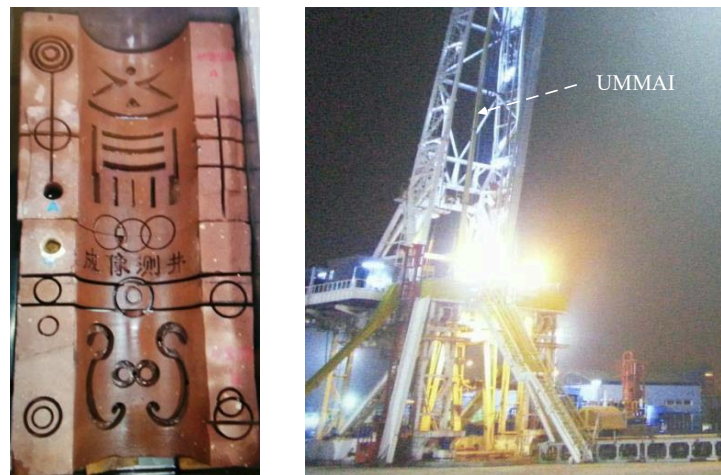


**Figure 10.** The field test setup of UMMAI. The **left** is patterns on the simulated borehole wall. The **right** is the test scenario of UMMAI.

In the first test, the simulated borehole is filled with oil-based mud. UMMAI moves from 8.4 to 11.1 m in depth and collects the resistance samples from 15 receiver electrodes on 6 pads, as shown in Figure 3.

After the samples are collected, the samples from different electrodes on the same pad are aligned first to eliminate the depth differences between electrodes. Then the samples from different pads are aligned to eliminate the depth differences between pads. After the alignment processing is finished, the background signal in the samples is removed through an average filter, and the modulus and phases of filtered samples are used for imaging.

The errors associated to the resistivity measurements during the field experiment are mainly caused by depth differences between electrodes, depth differences between pads and filter artifacts. The depth differences are eliminated in the alignment processing and the influence of filter artifacts can be suppressed to acceptable level by optimizing filter parameters. The modulus and phases of filtered samples are illustrated in Figures 11 and 12.

As shown in Figure 11, the patterns on the borehole wall can be imaged clearly with 200 kHz excitation signal in oil-based mud environment. At the depth of 9.13 m, a horizontal notch with a width of 8 mm can be distinguished. The amplitude of samples ranges from 0 to 322. The results with 1 MHz excitation signal gives slightly worse image of patterns, with the amplitude of samples ranging from 48 to 246, the scope of which is smaller than that of 200 kHz. It is considered to be caused by the high frequency attenuation in receiver channels and the influence of filling mud, which reduces the signal-to-noise ratio at the receiver electrodes. When the excitation frequency increases to 5 MHz, this phenomenon becomes more obvious and the pattern image is unable to provide any information about the borehole wall, since the sample amplitude ranges from 88 to 89.

As shown in Figure 12, the patterns on the borehole wall can also be imaged clearly using sample phases with 200 kHz and 1 MHz excitation signals, which agrees well with the results in Figure 11. The pattern image using sample phases with 5 MHz in Figure 12 performs better than that in Figure 11, in which several patterns can be distinguished.

In the second test, the simulated borehole is filled with water-based mud. UMMAI moves from 3.8 m to 6.8 m. The align operations and average filter are also applied over the samples. The modulus and phases of filtered samples are illustrated in Figures 13 and 14.

As shown in Figure 13, the patterns on the borehole wall can be imaged clearly with 200 kHz and 1 MHz excitation signals in water-based mud environment. At the depth ranging from 5.27 to 5.4 m, three horizontal notch with a width of 10 mm can be distinguished. Owing to the lower resistivity of water than oil, the amplitude of samples in 200 kHz and 1 MHz ranges from 0 to 614, and from 84 to 558, respectively, which are larger than those in Figure 11. Although the results with 5 MHz excitation signal still has the worst performance in Figure 13, it behaves better than that in Figure 11, since more

pattern details with 5 MHz excitation signal in Figure 13 are revealed, especially at depths from 5.8 m to 6.8 m. The sample amplitude with 5 MHz ranges from 205 to 369. The images in Figure 14 demonstrates consistent results with those in Figure 13.

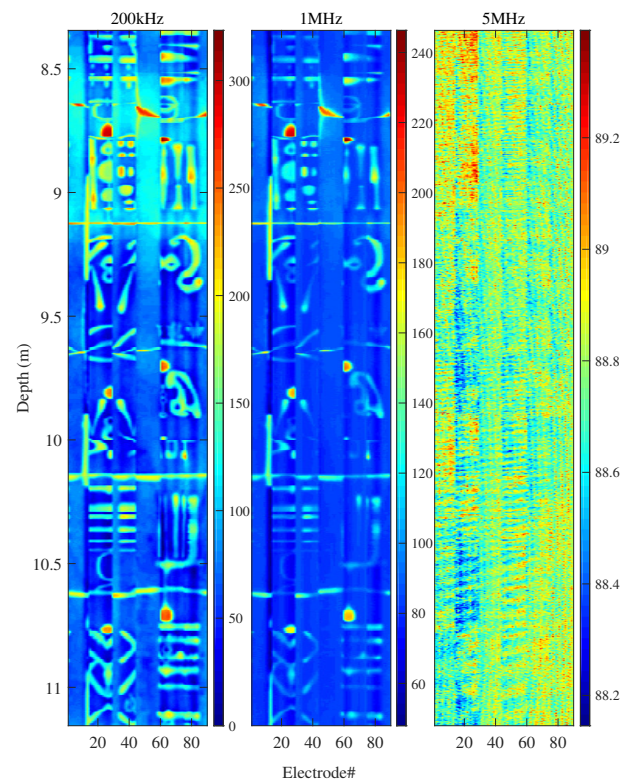


**Figure 11.** The imaging result of borehole wall patterns with UMMAI sample modulus in the first test, while the borehole is filled with oil-based mud.

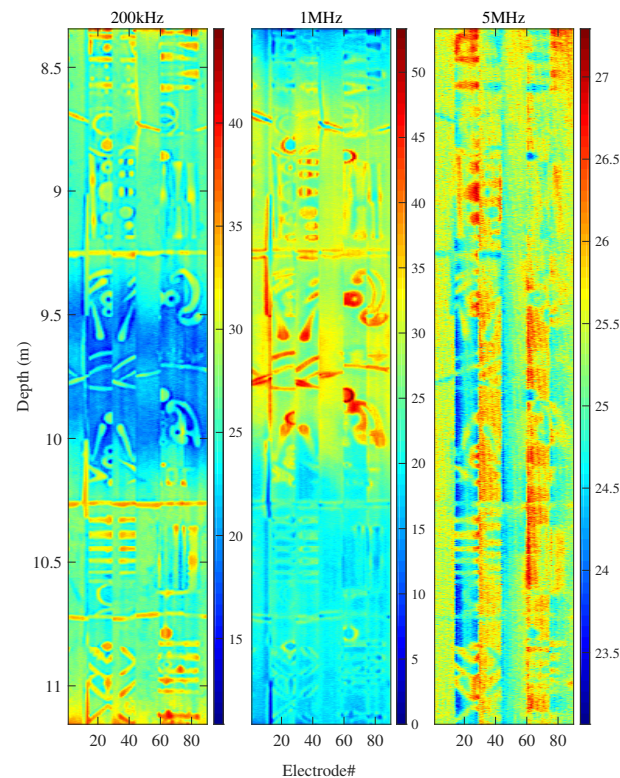


**Figure 12.** The imaging result of borehole wall patterns with UMMAI sample phases in the first test, while the borehole is filled with oil-based mud.

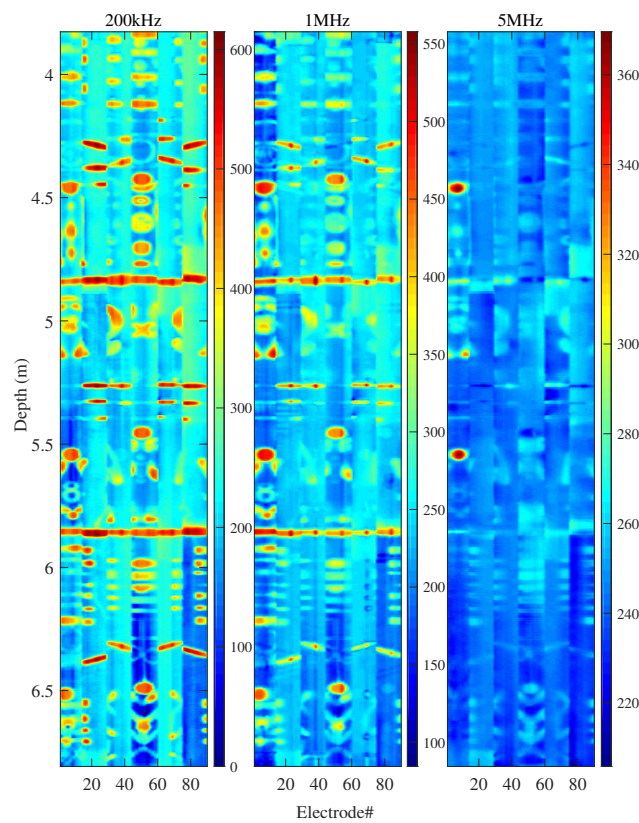


**Figure 13.** The imaging result of borehole wall patterns with UMMAI sample modulus in the second test, while the borehole is filled with water-based mud.

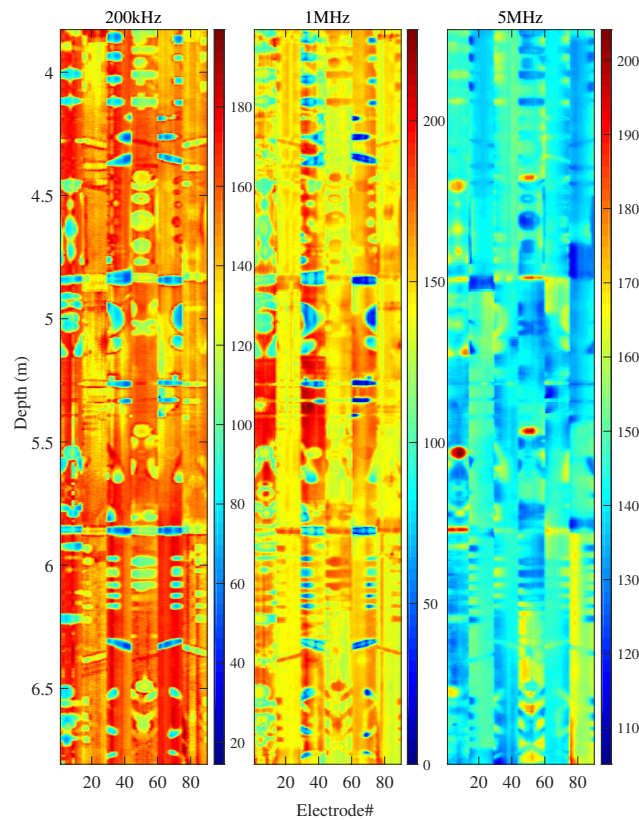


**Figure 14.** The imaging result of borehole wall patterns with UMMAI sample phases in the second test, while the borehole is filled with water-based mud.

Since the stratum impedance is frequency dependent, the sample amplitude will change in different magnetic fields. Moreover, the gap mud impedance between receiver electrode and stratum,  $Z_{Rn}$ , will also change in different environments, which will introduce changes in the measured impedance  $Z_{Mn}$ . The increase of working frequency leads to increase in the stratum impedance and gap mud impedance, which will reduce the current flowing the sample resistor and decrease the sample amplitudes. The reduced signal-to-noise ratio in higher working frequency environment will influence the imaging quality.

In the third test, the simulated borehole is filled with water-oil mixed mud. UMMAI moves from 10.9 m to 12 m. The same align operations and average filter are applied over the samples. The modulus and phases of filtered samples are illustrated in Figures 15 and 16.

As shown in Figure 15, the patterns on the borehole wall can also be imaged clearly with 200 kHz and 1 MHz excitation signals in water-oil mixed mud environment. At the depth ranging from 11.4 m to 11.6 m, four horizontal notches with a width of 8 mm can be distinguished. The amplitude of samples in 200 kHz and 1 MHz ranges from 0 to 398, and from 126 to 214, respectively, which are larger than those in Figure 11 and smaller than those in Figure 13. The results with 5 MHz excitation signal also gives acceptable image of patterns. The sample amplitude with 5 MHz ranges from 136 to 201. The images in Figure 16 demonstrates consistent results with those in Figure 15.

Since the UMMAI system is a multi-frequency working system, the resolution performance of UMMAI is comprehensively evaluated with amplitude and phase images with all working frequencies. The above results show that UMMAI can provide high resolution images in different mud environments.

According to the public literatures from Baker Hughes [30] and Halliburton [31], the vertical and azimuthal resolution of STAR imager is about 0.2 inch (5 mm), and its applicable mud resistivity range is from 0.01  $\Omega$ /m to 10  $\Omega$ /m, which is not suitable for oil-based mud environment. The resolution of EMI and StrataXaminer is about 0.2 in (5 mm), and they are only applicable in an oil-based mud environment.

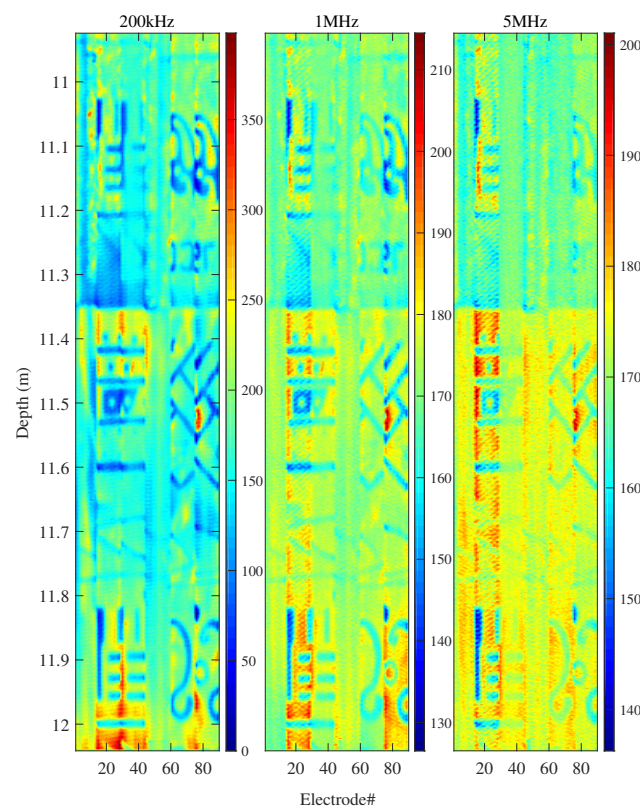


**Figure 15.** The imaging result of borehole wall patterns with UMMAI sample modulus in the third test, while the borehole is filled with water-oil mixed mud.

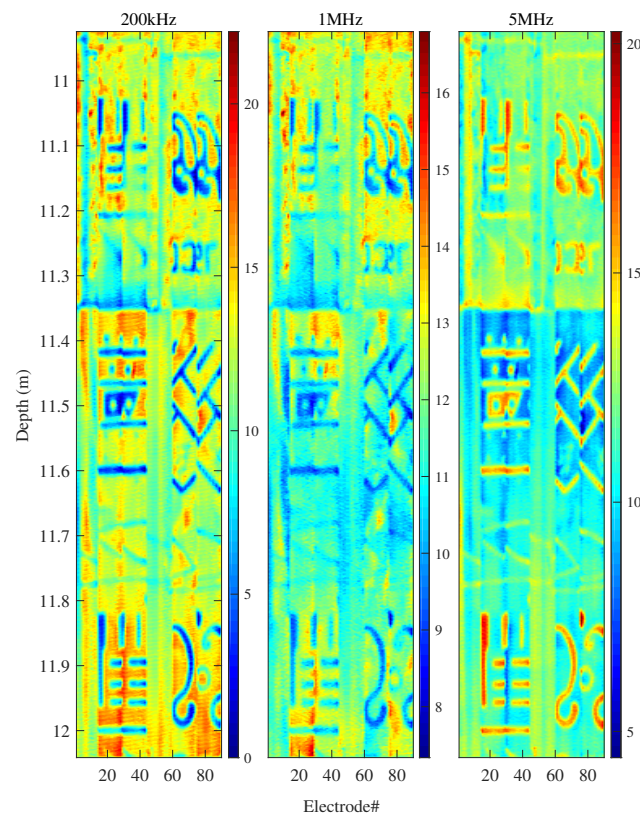


**Figure 16.** The imaging result of borehole wall patterns with UMMAI sample phases in the third test, while the borehole is filled with water-oil mixed mud.

In the field tests of UMMAI, limited to the minimum notch width in the test fields, several horizontal notches with a width of 8 mm can be distinguished in Figures 11 and 15. Therefore, UMMAI is regarded to own a resolution better than 8 mm and has comparable imaging performance with mainstream commercial logging equipments, which is suitable and universal in multiple mud environments.

#### 4. Conclusions

To obtain diverse high-resolution subsurface formation information in various logging scenarios, a universal multi-frequency micro-resistivity array imaging (UMMAI) system is developed and verified. The methodology and modeling of UMMAI are established and the UMMAI hardware design is presented. Several lab tests are conducted over UMMAI and the result verifies large dynamic range, good linearity of transceivers and excitation signal diversity in UMMAI, which enable UMMAI present abundant amplitude–frequency characteristics response images and phase–frequency characteristics response images of subsurface formations at the same time. Three field tests analysis of UMMAI show that it can give satisfactory credible formation images with high resolution, which is suitable for subsurface formation discrimination and useful for reservoir identification.

**Author Contributions:** Conceptualization, H.Y. and T.L.; methodology, H.Y. and T.L.; software, H.Y., T.L. and S.Y.; validation, H.Y. and T.L.; formal analysis, H.Y.; writing—original draft preparation, H.Y. and Y.L.; writing—review and editing, H.Y. and N.L. All authors have read and agreed to the published version of the manuscript.

**Funding:** This work is supported in part by the National Natural Science Foundation of China under Grants 62171099 and U19A2056, and in part sponsored by Natural Science Foundation of Sichuan, China, under grants 2022NSFSC0862, 2022NSFSC0888 and 2022NSFSC0546 and in part by the Fundamental Research Funds for the Central Universities under Grant ZYGX2020J002.

**Data Availability Statement:** The datasets are available from the authors on reasonable request.

**Conflicts of Interest:** The authors declare no conflict of interest.

## References

1. Liu, J.; Zhuo, J.; Jiang, W.; Liu, Q.-H. 3-D Numerical Mode Matching Method for Off-Centered Electromagnetic Well Logging Tools in Noncircular Vertical Borehole and Invasion Zones in Multilayered Media. *IEEE Trans. Geosci. Remote Sens.* **2022**, *60*, 1–13. [[CrossRef](#)]
2. Zhang, W.; Li, Z.; Wu, T.; Yao, Z.; Qiu, A.; Li, Y.; Shi, Y. Fracture Identification in Well Logging Images: Two-Stage Adaptive Network. *IEEE Trans. Instrum. Meas.* **2022**, *71*, 1–12. [[CrossRef](#)]
3. Saavedra, L.; Rosa, G.-S.; Bergmann, J.-R. A Combined Mode-Matching Technique and Born Approximation Method to Model Well-Logging Sensors in Non-Axisymmetric Boreholes. *IEEE Access* **2021**, *9*, 84364–84374. [[CrossRef](#)]
4. Tian, B.; Wang, L.; Kashiwaya, K.; Koike, K. Combination of Well-Logging Temperature and Thermal Remote Sensing for Characterization of Geothermal Resources in Hokkaido, Northern Japan. *Remote Sens.* **2015**, *7*, 2647. [[CrossRef](#)]
5. Abdi, O.; Uusitalo, J.; Kivinen, V.-P. Logging Trail Segmentation via a Novel U-Net Convolutional Neural Network and High-Density Laser Scanning Data. *Remote Sens.* **2022**, *14*, 349. [[CrossRef](#)]
6. Sun, D.; Li, X.; Cao, Z.; Yong, J.; Zhang, D.; Zhuang, J. Acoustic Robust Velocity Measurement Algorithm Based on Variational Bayes Adaptive Kalman Filter. *IEEE J. Ocean. Eng.* **2021**, *46*, 183–194. [[CrossRef](#)]
7. Song, X.; Zhao, Y.; Dykstra, J. Active Damping of Acoustic Ringing Effect for Oil Well Sonic Logging System. *IEEE Trans. Ind. Electron.* **2017**, *64*, 3423–3432. [[CrossRef](#)]
8. Ao, Y.; Lu, W.; Hou, Q.; Jiang, B. Synthesize Nuclear Magnetic Resonance T2 Spectrum From Conventional Logging Responses With Spectrum Regression Forest. *IEEE Geosci. Remote Sens. Lett.* **2021**, *18*, 1726–1730. [[CrossRef](#)]
9. Zhu, J.; Wang, H.; Zhou, K.; Lin, T. A Design Scheme of Receiving System of Small-Diameter Nuclear Magnetic Resonance Logging Tool. *IEEE Trans. Instrum. Meas.* **2021**, *70*, 1–10. [[CrossRef](#)]
10. Bai, Y.; Zhan, Q.; Wang, H.; Chen, T.; He, Q.; Hong, D. Calculation of Tilted Coil Voltage in Cylindrically Multilayered Medium for Well-Logging Applications. *IEEE Access* **2020**, *8*, 30081–30091. [[CrossRef](#)]
11. Hu, X.; Fan, Y.; Deng, S.; Yuan, X.; Li, H. Electromagnetic Logging Response in Multilayered Formation with Arbitrary Uniaxially Electrical Anisotropy. *IEEE Trans. Geosci. Remote Sens.* **2020**, *58*, 2071–2083. [[CrossRef](#)]
12. Chen, J.; Yue, W.; Li, C.; Zeng, F. Extracting Reflected Waves From Acoustic Logging Data Based on the Shearlet Transform. *IEEE Geosci. Remote Sens. Lett.* **2019**, *16*, 1688–1692. [[CrossRef](#)]
13. Aeron, S.; Bose, S.; Valero, H.-P. Robust Detection and Estimation for Logging While Drilling Monopole Acoustic Data. *IEEE Trans. Signal Process.* **2015**, *63*, 3062–3075. [[CrossRef](#)]
14. Wang, B.; Zhang, K. Direct Inversion Algorithm for Shear Velocity Profiling in Dipole Acoustic Borehole Measurements. *IEEE Geosci. Remote Sens. Lett.* **2018**, *15*, 828–832. [[CrossRef](#)]
15. Gaunkar, N.P.; Nlebedim, I.C.; Bulu, I.; Mina, M.; Hadimani, R.L.; Song, Y.Q.; Jiles, D.C. Broadband Analysis of Response From Magnetic Cores Used in Inductive Sensors for Pulsed Nuclear Magnetic Resonance Applications. *IEEE Trans. Magn.* **2016**, *52*, 1–4. [[CrossRef](#)]
16. Xu, X.; Kong, X.; Zhang, J.; Wang, G.; Bao, Z.; Yu, H.; Xu, Z. Optimization of Inside-Out Nuclear Magnetic Resonance Sensor with Logging-While-Drilling Tool Specification and Experimental Validation. *IEEE Trans. Instrum. Meas.* **2022**, *71*, 1–10.
17. Lehmensiek, R.; de Villiers, D.-I.-L. Optimization of Log-Periodic Dipole Array Antennas for Wideband Omnidirectional Radiation. *IEEE Trans. Antennas Propag.* **2015**, *63*, 3714–3718. [[CrossRef](#)]
18. Zhong, Y.; Wang, H.; Huang, W.F.; Xu, W.; Xu, J.; Dai, J.; Liu, Q.H. A Hybrid Loop-Tree FEBI Method for Low-Frequency Well Logging of 3-D Structures in Layered Media. *IEEE Trans. Geosci. Remote Sens.* **2022**, *60*, 1–9.
19. Yan, B.; Zhu, W.; Zhuang, X.; Liu, L.; Fang, G. Miniature Three-Axis Induction Magnetometer for Borehole Logging. *IEEE Magn. Lett.* **2019**, *10*, 1–4. [[CrossRef](#)]
20. Hu, Y.; Guo, R.; Jin, Y.; Wu, X.; Li, M.; Abubakar, A.; Chen, J. A Supervised Descent Learning Technique for Solving Directional Electromagnetic Logging-While-Drilling Inverse Problems. *IEEE Trans. Geosci. Remote Sens.* **2020**, *58*, 8013–8025. [[CrossRef](#)]
21. Yan, L.; Zeng, S.; Chen, J. 2-D Pixel-Based Inversion for Simultaneous Reconstruction of Resistivity and Dielectric Constant From Electromagnetic Logging-While-Drilling Measurements. *IEEE Trans. Geosci. Remote Sens.* **2022**, *60*, 1–14.
22. Yan, L.; Jin, Y.; Qi, C.; Yuan, P.; Wang, S.; Wu, X.; Huang, Y.; Chen, J. Deep Learning-Assisted Real-Time Forward Modeling of Electromagnetic Logging in Complex Formations. *IEEE Geosci. Remote Sens. Lett.* **2022**, *19*, 1–5.
23. Rosa, G.-S.; Bergmann, J.-R.; Teixeira, F.-L. A Perturbation Method to Model Electromagnetic Well-Logging Tools in Curved Boreholes. *IEEE Trans. Geosci. Remote Sens.* **2018**, *56*, 1979–1993. [[CrossRef](#)]
24. Xing, G.; Wang, H.; Ding, Z. A New Combined Measurement Method of the Electromagnetic Propagation Resistivity Logging. *IEEE Geosci. Remote Sens. Lett.* **2008**, *5*, 430–432. [[CrossRef](#)]
25. Zhang, Y.; Xu, L.; Cao, Z. Optimization of the Electromagnetic Wave Resistivity Tool in Logging While Drilling. In Proceedings of the 2013 IEEE International Conference on Imaging Systems and Techniques (IST), Beijing, China, 22–23 October 2013; pp. 160–163.
26. Liu, X.; Liu, F.; Chen, J.; Zhao, Z.; Wang, A.; Lu, Z. Resistivity Logging Through Casing Response of Inclined Fractured Formation. *IEEE Trans. Geosci. Remote Sens.* **2018**, *56*, 4919–4929. [[CrossRef](#)]
27. Ren, Y.; Gong, R.; Feng, Z.; Li, M. Valuable data extraction for resistivity imaging logging interpretation. *Tsinghua Sci. Technol.* **2020**, *25*, 281–293. [[CrossRef](#)]

28. Wang, L.; Li, H.; Fan, Y. Bayesian Inversion of Logging-While-Drilling Extra-Deep Directional Resistivity Measurements Using Parallel Tempering Markov Chain Monte Carlo Sampling. *IEEE Trans. Geosci. Remote Sens.* **2019**, *57*, 8026–8036. [[CrossRef](#)]
29. Pardo, D.; Torres-Verdin, C.; Demkowicz, L. A 2D and 3D hp-Finite Element Method for Simulation of Through Casing Resistivity Logging Instruments. In Proceedings of the 2006 IEEE Antennas and Propagation Society International Symposium, Albuquerque, NM, USA, 9–14 July 2006; pp. 1769–1772.
30. Available online: <https://www.bakerhughes.com/evaluation/wireline-openhole-logging/wireline-imaging/star-imager-service> (accessed on 25 June 2022).
31. Available online: <https://www.halliburton.com/en/products/strataxaminer> (accessed on 25 June 2022).